Accurate control of friction with nanosculptured thin coatings: Application to gripping in microscale assembly

Philippe Stempflé[a)], Aurélien Besnard[b)], Nicolas Martin[a)], Anne Domatti[a)], Jamal Takadoum[a)]

[a)] *Institut FEMTO-ST (UMR CNRS 6174 - Université de Franche Comté - CNRS - ENSMM - UTBM), ENSMM 26 Chemin de l'Epitaphe, F-25030 Besançon Cedex, FRANCE*

[b)] *LaBOMaP, Arts et Métiers ParisTech de Cluny, Rue Porte de Paris, F-71250 Cluny, FRANCE*

Abstract

Chromium thin films were sputter deposited implementing the GLancing Angle Deposition (GLAD) method, which is a thin film deposition technique where the incident vapor flux - composed of atoms and molecules from gas phase - strikes onto the substrate at tilted angles α. Oriented chromium columns were produced with various column angles β (from 0 to 60°) closely linked to the sputtering pressure and incidence angle α. Three sputtering pressures of 0.11, 0.40 and 0.53 Pa were used. Incidence angle α of the sputtered particles was systematically changed from 0 to 80°. Tribological properties were investigated as a function of these operating parameters. Results reveal that the tribological behaviour is strongly correlated with the structure and especially the growth mechanism of the films, which are both linked with the operating sputtering parameters. Thus, at the lowest sputtering pressure (0.11 Pa), gradual variations of the tribological properties and wettability are observed as a function of the incidence angle α, which are interresting for tailoring surfaces displaying a gradient of wettability. In contrast, at higher sputtering pressures (>0.2 Pa), local variations of static friction coefficient, wettability and lateral contact stiffness are systematically observed as a function of the column angle β - and then the incidence angle α . Basically, these results enable to tailor tribological properties by tuning the incidence angle α in order to control the transition from sticking to sliding in micro-gripping.

Keywords: MEMS, friction control, nanosculptured thin coatings, micro-gripping,

1. Introduction

In microassembly, two approaches are currently considered [1]: (i) the self-assembly paradigm [2, 3, 4] in which surface effects are used to organize and assemble structures mainly up to a few micrometers, and (ii) the microrobotic assembly [1, 5], based on the miniaturization of the actuation, high resolution micromanipulators and gripping devices (Fig. 1a), more dedicated to mesoscopic sized components (between a few micrometers and a few millimeters). This one is well suitable for assembling MEMS components where the main challenging issues concern the handling of small components (mainly down to about 10 µm). Current research in this field includes: (i) the development of new strategies to pick up, to handle, and to release micro-components as for instance microassembly in dry and liquid medium [6]; and (ii) the development of new types of surfaces [7, 8, 9, 10, 11, 12, 13], which would enable to control separately the various components of friction occurred in dry medium microassembly. In this framework, whereas adhesive components [14, 15, 16, 17] and capillary effects [1, 11, 13, 18] (see Fig. 1b) are generally controlled by grafting self-assembly molecules on grippers in order to reduce their surface tension [15, 19], mechanical components of friction - *i.e* static and dynamic friction coefficients and especially static to dynanic coefficient ratio - could be controlled by means of highly porous nanosculptured thin films (Fig. 1c) purposely tailored to achieve desired tribological properties [9, 13, 20, 21, 22, 23].

Email address: philippe.stempfle@ens2m.fr (Philippe Stempflé[a)], Aurélien Besnard[b)], Nicolas Martin[a)], Anne Domatti[a)], Jamal Takadoum[a)])

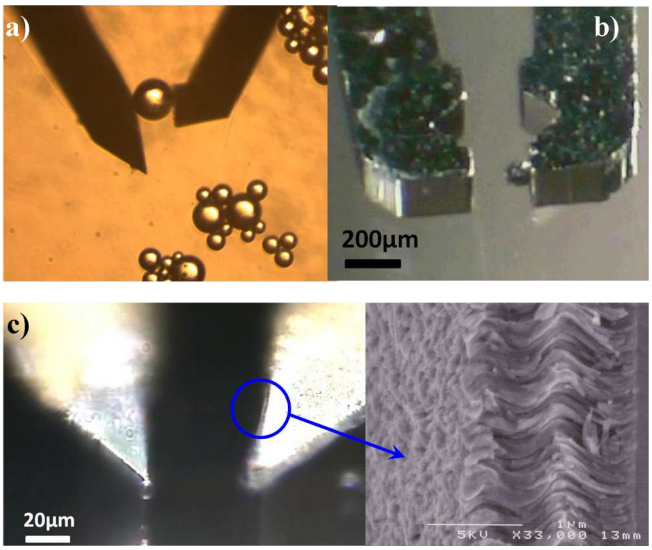

Figure 1: Optical views of micro-grippers used in microassembly [*e.g.*,42, 43]: (a) the size of the handled object is about 40 µm; (b) capillary effects in micro-assembly: the handled object remains stuck on the bare microgripper; (c) nanosculptured thin film that is coated on the gripper's fingers can prevent these capillary effects, and moreover it enables to control the transition from sticking to sliding by tailoring its microarchitecture

GLancing Angle Deposition (GLAD) method – first reported in 1959 [24] and later by Robbie *et al* [25] – is an attractive physical vapour deposition method to fabricate complex 1D, 2D or 3D nanostructured columnar thin films [26, 27, 28] including nanopillars [23, 27, 28, 29, 30], zigzag nanocolumns [20, 31], and nanospirals [32]. This method is based on the change of location of the vapour source relative to the columns during growth. Basically, the source is not moved but rather the substrate, which can be tilted or/and rotated along its central axis (Fig. 2). Thus, two degrees of freedom can be adjusted: (i) a rotation axis at an angle α, which allows to vary the incidence angle of the particles flux, and (ii) a rotary axis at an angle ϕ also called azimuthal angle, which indirectly modifies the position of the particles source. The GLAD technique takes advantage of the shadowing effect created by a tilted substrate relative to the normal incidence and a change of the material flux through a rotation of the same substrate during the deposition. As a result, by favouring the directional growth of the columns and controlling their structure, it is possible to produce various kinds of nanoarchitecture (Fig. 3) displaying a widening spectrum of physico-chemical properties of materials including their state of stress [29, 33, 34], density [35], optical [22], electrical [35] and mechanical behaviours [23, 28, 30, 32]. Besides, topography [22, 27, 36, 37] and wettability of films can also be controlled by the operating parameters - *i.e* sputtering pressure, incidence angle α and column angle β.

So, the aim of this work is to study how these operating parameters can influence the structure, the density, the mechanical properties and finally the tribological properties of GLAD films under low contact pressure (150 MPa) and low velocity (0.1 mm/s) as met in classical microassembly grippers [1, 5, 38]. For this purpose, chromium thin films (thickness about 850 nm and RMS: 8.7± 3.6 nm) were sputter deposited implementing the GLAD method on silicon wafers by varying both the sputtering pressure (from 0.11 to 0.53 Pa) and the incidence angle α of the sputtered particles from 0 to 80°. Oriented chromium columns were produced with various column angles β (from 0 to 60°) closely linked to the sputtering pressure and incidence angle α. Note that the panel of architectures produced by GLAD method is not solely restricted to metallic compounds, but ceramics [39], and semiconducting [40] or alloyed materials [41] can be grown. Thus, chromium allows the synthesize of attractive compounds for mechanical performances, especially metalloid materials such as some chromium nitride phases CrN or Cr_2N. However, in this work, pure chromium films was preferred to alloyed materials or other complex compounds because the sputtering mechanisms of particles are largely simplified and easier to simulate in order to understand the possible relationships between the growth, the structure and the tribological properties of GLAD films.

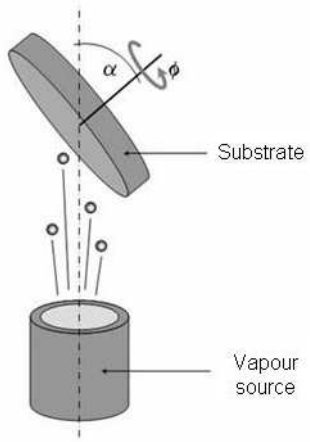

Figure 2: Basic principle of the experimental device used for the GLAD technique. The substrate is positioned in front of the vapour source on a substrate holder, which can be tilted according to an angle α compared to the normal to the substrate. Moreover, it can be animated by a rotation ϕ along an axis centred on the substrate.

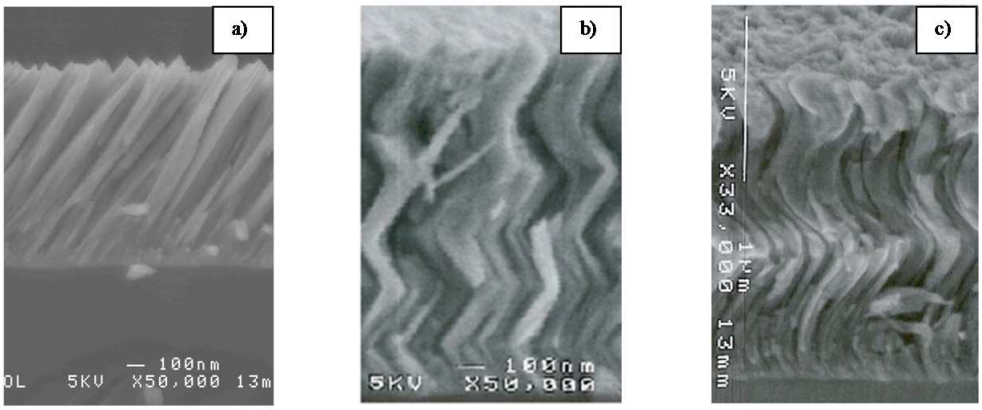

Figure 3: Observation by SEM of the cross section of: a) inclined ; b) zig-zag ; c) helical columnar structure of chromium films deposited on (100)Si by magnetron sputtering [33]

2. Experimental part

2.1. Deposition of the nanosculptured chromium thin films

Chromium thin films were deposited on (100) silicon substrates by dc magnetron sputtering from chromium metallic target (purity 99.7 at.%). The metallic target was sputtered with a constant current density $J_{Cr} = 200\,A.m^{-2}$ in argon atmosphere. The substrates were grounded and kept at room temperature. Argon mass flow rate was set constant in order to reach a sputtering pressure of 0.11, 0.40 or 0.53 Pa (pumping speed was maintained at S = 10 $L.s^{-1}$). The deposition time was ajusted in order to deposit a constant thickness close to 900 nm. This latter was checked after deposition by profilometry. The home-made GLAD substrate holder allowed an orientation change of the incidence angle of the particles flux α from 0 to 90°.

2.2. Thin films characterization

2.2.1. Structure and density

The crystallographic structure was investigated by X-ray diffraction (XRD) using monochromatized CoK_α radiation with a Bragg-Brentano configuration $\theta/2\theta$. The Debye-Scherrer method was used to calculate the crystallite grain size. Column angle β was measured from scanning electron microscopy (SEM) observations on the fractured cross-section of the films deposited on silicon substrates. Density of the films was calculated as a function of the incidence angle α of the sputtered particules and for the three different pressures using Paik's relationships [44]. Density ξ of oriented thin films produced by GLAD, can be related to the incidence angle α of the particles flux by:

$$\xi = \frac{\xi_{\alpha=0^\circ}}{1 + c\tan(\alpha)} \tag{1}$$

where $\xi_{\alpha=0^\circ}$ is the density of the film ($kg.m^{-3}$) deposited at an incidence angle $\alpha = 0^\circ$ and c is a constant, which is proportional to the ratio of the shadowing step height to the column thickness. At first, we suppose that the density of the bulk material ξ_0 is the same as the density of the film deposited at an incidence angle $\alpha = 0^\circ$ (*i.e* $\xi_0 = \xi_{\alpha=0}$). Parameter c depends on the nature of the sputtered materials and the deposition conditions, especially the sputtering pressure. Films' density *vs.* incidence angle was computed for the three involved pressure : 0.11, 0.40 and 0.53 Pa (Fig. 4).

An abrupt drop of the density can be noticed for incidence angles higher than 60° where the shadowing effect at the atomic scale becomes significant. For grazing incidence angles ($\alpha > 80^\circ$), a high porous structure is obtained since the density of the film is few tens % of the bulk. Consequently, to get some knowledge of the film's density, evolution as a function of the incidence angle α allows some close correlations between structural characteristics (*e.g.* the growth of a porous architecture) and tuneable mechanical [28] or electrical properties [35].

2.2.2. Topographical analysis

Thin films exhibit self-affine properties in a certain range of scales [36, 37, 45]. Self-affinity is a generalization of self-similarity, which is the basic property of most of the deterministic fractals [46]: a part of self-affine object is similar to whole object after anisotropic scaling. Thus, many randomly rough surfaces are assumed to belong to the random objects that exhibit the self-affine properties [47, 48]. Fractal analyses of the self-affine random surfaces using AFM or profilometer are often used to study and compare these surfaces, which have the same thickness and roughness [37, 49, 50, 51].

Different methods of fractal analysis are reported in the literature [16, 18, 37, 45, 46, 48, 49, 50, 51, 52, 53, 54]. Each one displays its systematic error but results obtained by any method provide informations about the degree of complexity or fragmentation of the surfaces [45]. However, the measurement accuracy can strongly be affected by the chosen method [49]. Thus, in this work, fractal dimension (D_f) is computed by using a *cube counting method* [37, 49] - implemented within the SPM data analysis software Gwyddion *(http://gwyddion.net)* - which is directly derived from the well-reliable *box-counting* approach [48]. The algorithm is based on the following steps: a cubic lattice with lattice constant l is superimposed on the z-expanded surface. Initially l is set at $\frac{X}{2}$ (where X is length of edge of the surface), resulting in a lattice of 8 cubes. Then $S(l)$ is the number of all cubes that contain at least one pixel of the image. The lattice constant

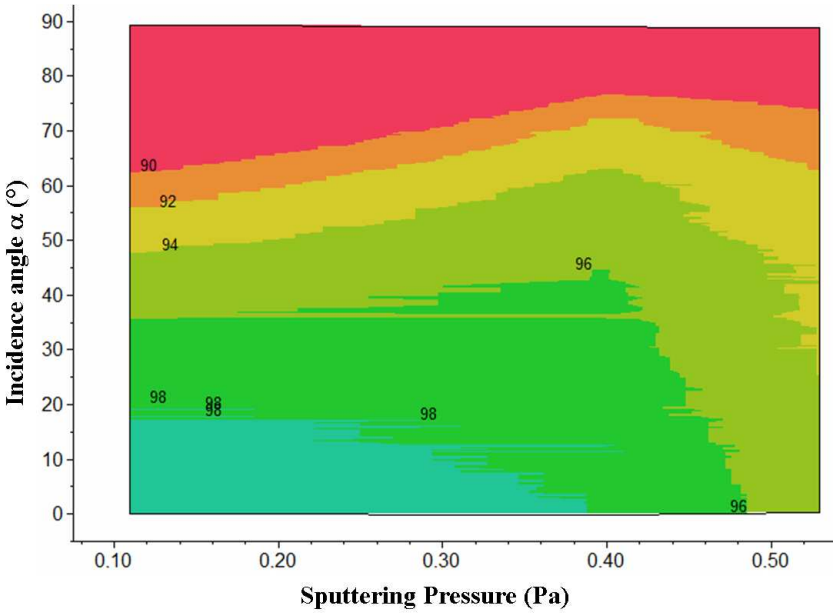

Figure 4: Computed relative density of chromium thin films (in %) *vs.* incidence angle of the particles flux according to the Paik's model for different sputtering pressures [44]

l is then reduced stepwise by factor of 2 and the process repeated until l equals to the distance between two adjacent pixels. The slope of a plot of $\log(S(l))$ versus $\log(1/l)$ gives the fractal dimension D_f directly (Fig. 5a).

Since results of fractal analysis can strongly be influenced by the tip convolution of the AFM analysis (*Digital Instruments Nanoscope III Dimension 3000),* this one was checked beforehand [49, 51]. Besides, fractal's results were also compared on larger scales by using a phase shifting interferometric profilometer *ATOS MICROMAP 570* (λ = 520 nm, spatial and vertical resolutions are 0.5 µm and 0.02 nm, respectively) in order to compute the systematic error: around 3%. (Fig. 5b). Finally average value of $\overline{D}_f$ was computed from data compiled from the whole AFM and interferometric pictures.

2.3. Nanotribological setup

In this work, tribological experiments are carried out for modelling the two critical steps of microgripping (i.e., pick-up and release, respectively) when sliding and/or adhesion occur between the handled object and the gripper [1, 38]. So, the experimental device is a *ball-on-disc* nanotribometer manufactured by *CSM Instruments* (*Switzerland*) [55]. Fig. 6 displays the link between the microgripping (Fig. 6a) and the tribological test (Fig. 6b): (i) the gripper is modelled by the flat sample, which is coated by the various GLAD films ; (ii) the handled object is modelled by a Si_3N_4 ball which is glued on the pin. Besides, the latter is mounted on a stiff lever (Fig. 6c), designed as a frictionless force transducer (K_x= 265.1 Nm^{-1}; K_z = 152.2 Nm^{-1}). During the test, the ball is loaded onto the flat sample with a precisely known force using closed loop. The friction force is determined by measuring the deflection of the elastic arm (low load range down to 50 µN). The load and friction resolutions are about 1 µN.

As shown in Fig. 7, the nanotribometer is set within a glove box in order to control both the temperature (22°C) and the relative humidity (RH 35%) and so, any additional capillary effects that could occur during the tests. The normal load (10 mN) and the ball's diameter ($\phi 4\,mm$) are accurately chosen for limiting the contact pressure at 150 MPa, which is usually met in microgripping [*e.g.*, 1].

All tests are carried out in linear reciprocating mode both in the direction *"parallel"* and *"perpendicular"* to the orientation of the columns, *"with"* and *"against"* the tilt axis of the columns, in order to notice any effect of the column angle on the friction behaviour. As reported in Fig. 8, two kinds of tests are carried out depending on the oscillation amplitude of the displacement.

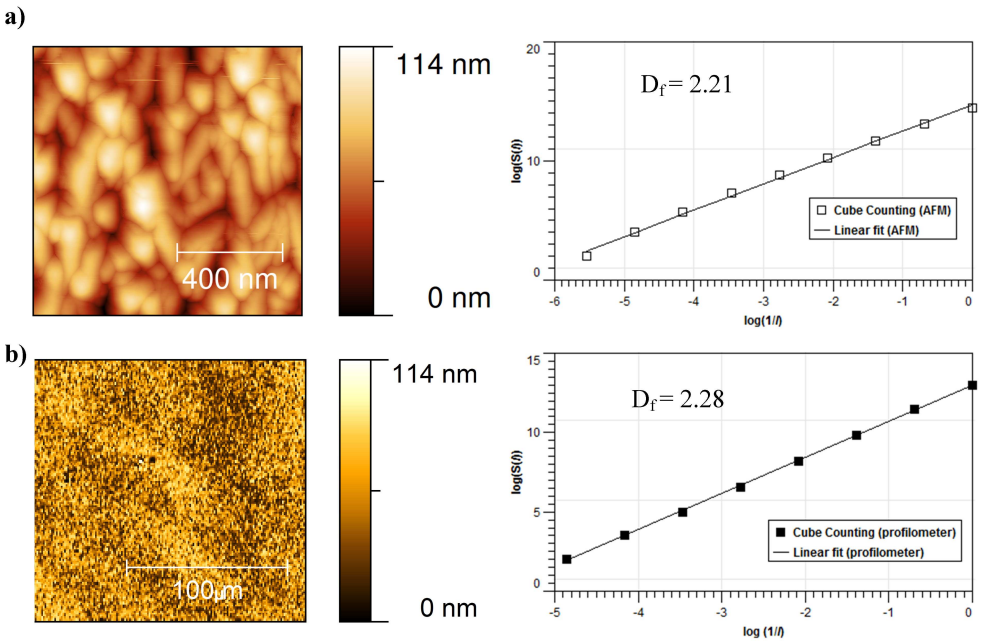

Figure 5: Examples of the fractal dimension assessments for chromium films deposited with $\alpha = 80°$ and sputtering pressure of 0.11 Pa carried out on (a) an AFM map (1 µm): $D_f = 2.21$ and (b) an interferometric profilometer map (320 µm):$D_f = 2.28$

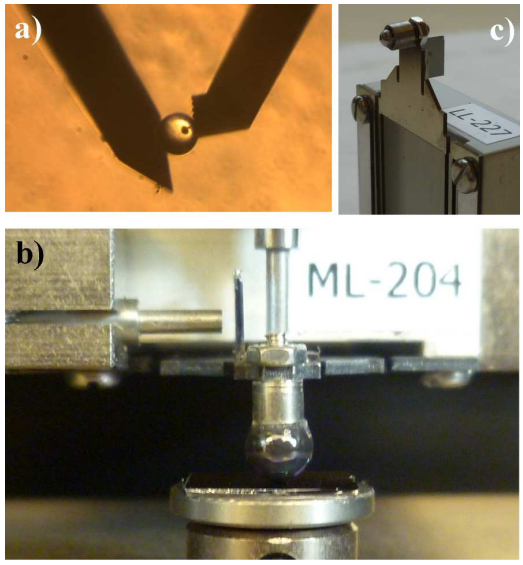

Figure 6: Link between the microgripping geometry (a) and the nanotribological test (b): The gripper is modelled by the flat sample coated by the GLAD film ; the handled object is modelled by the ball glued on the cantilever (c)

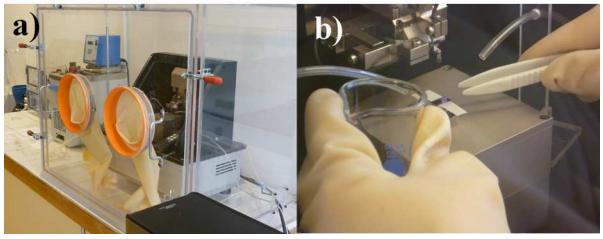

Figure 7: Nanotribometer in the environmental glove box

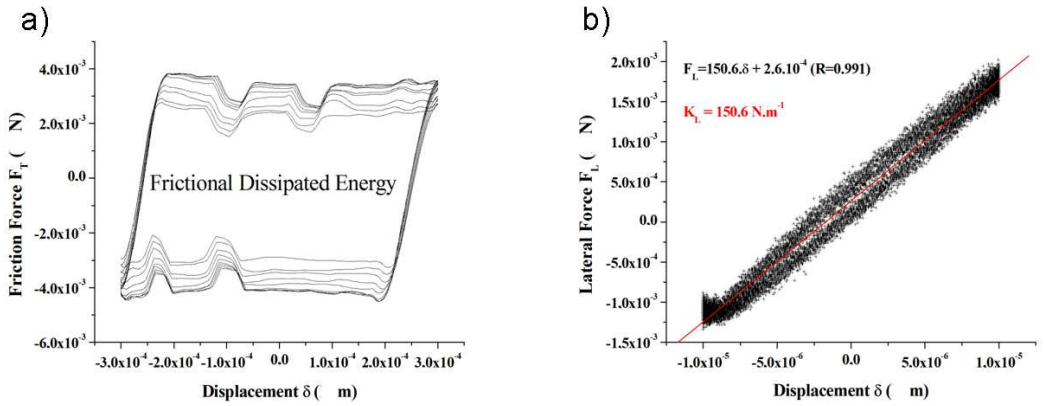

Figure 8: Tribological tests : a) in gross slip regime for measuring $\overline{\mu_s}$ and $\overline{\mu_d}$ on the whole of cycles b) in absence of sliding, the assessment of the slope of $F_T = f(\delta)$ when $\delta < a$ (with a, the hertz contact radius) gives the average *lateral contact stiffness* $\overline{k_L}$

- (i) When the oscillation amplitude is greatly higher than the contact radius (*i.e* $\delta \pm 0.5$ mm), a gross slip regime is observed (Fig. 8a) leading to assess both the average static ($\overline{\mu}_s$) and dynamic ($\overline{\mu}_d$) friction coefficient, and also the ratio $\frac{\overline{\mu}_s}{\overline{\mu}_d}$ particularly interesting to control the transition from sticking to sliding in microassembly. The average value of friction coefficients are computed by considering all the cycles of the tribological tests. Besides, possible wear can also be assessed. For this kind of test, the sliding velocity and the number of cycles are: 0.1 mm.s^{-1} and 10 cycles, respectively.

- (ii) When the oscillation amplitude is lower than the contact radius ($\delta \pm 10$ µm), no sliding is occurred (Fig. 8b). So, the coating is just submitted to a shear test, that enables to assess the *lateral contact stiffness* as reported by Mindlin *et al* [56]. The variations of the latter with the sputtering parameters (incidence angle α, sputtering pressure) provide informations about the mechanical properties of films. The *lateral contact stiffness* is the slope from the friction force *vs.* displacement (Fig. 8b). In this case the velocity and the number of cycles are 5 $\mu m.s^{-1}$ and 10 cycles, respectively.

3. Results and discussion

3.1. Morphology and structure of GLAD thin films

As expected by the structural zone model proposed by Thornton [57], films deposited according to our deposition conditions and with a perpendicular incidence of the particles flux ($\alpha = 0°$) exhibit a typical columnar microstructure. This kind of morphology corresponds to the transition zone of the Thornton's model since the sputtering pressure was 0.11, 0.40 and 0.53 Pa and the substrate temperature was a few tens of the chromium melting point (2173 K). Columns consist of inverted cone-like units capped by domes. Films produced with these operating conditions appear as a quite dense structure with columns width close to 100 nm. They are more or less separated by voided boundaries that are few nanometres wide. A similar columnar structure was produced for films prepared at sputtering pressure of 0.11, 0.40 and 0.53 Pa. Increasing the incidence angle α of the particles flux, inclined columns become separated and a much more porous and fibrous structure is produced as the incidence angle α increases and the sputtering pressure reduces down to 0.11 Pa. It is also worth of noticing that the column angle β is influenced by the sputtering pressure (Fig. 9).

As the incidence angle α tends to 90°, the column angle β asymptotically reaches 24° for 0.53 Pa whereas β tends to 35° for 0.40 Pa and β reaches 60° for 0.11 Pa. Thus, for the three sputtering pressures, β versus α well follows the empirical tangent rule ($\tan\alpha = 2\tan\beta$) up to an incidence angle α close to 60°, as commonly observed for several compounds [58]. Afterwards, a saturation of the column angle β occurs. It is mainly attributed to the mean free path of the sputtered particles and the sputtering emission (the angular distribution of sputtered atoms follows an undercosine law for energy ions lower than 1 keV [59]) peculiar

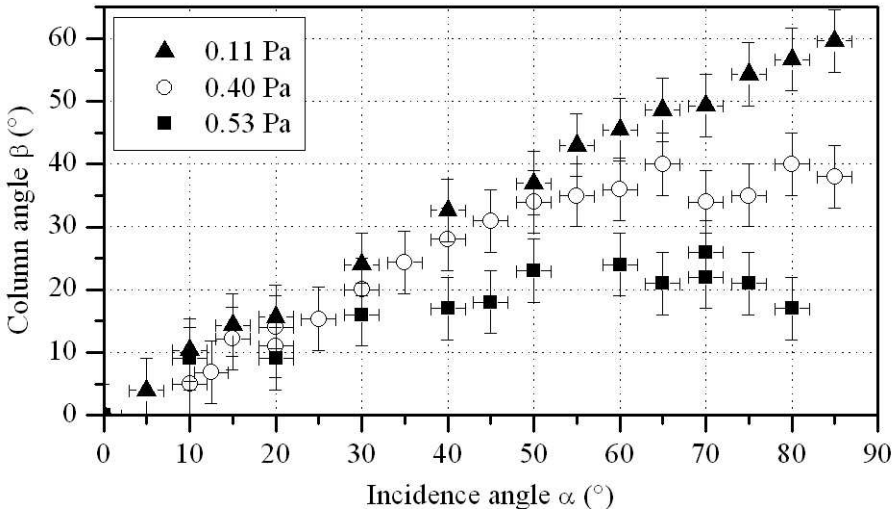

Figure 9: Evolution of the column angle β *vs.* incidence angle α in chromium thin films deposited by sputtering for three different argon pressures. Column angle β saturates close to 24 and 35° for sputtering pressure of 0.53 and 0.40 Pa, respectively

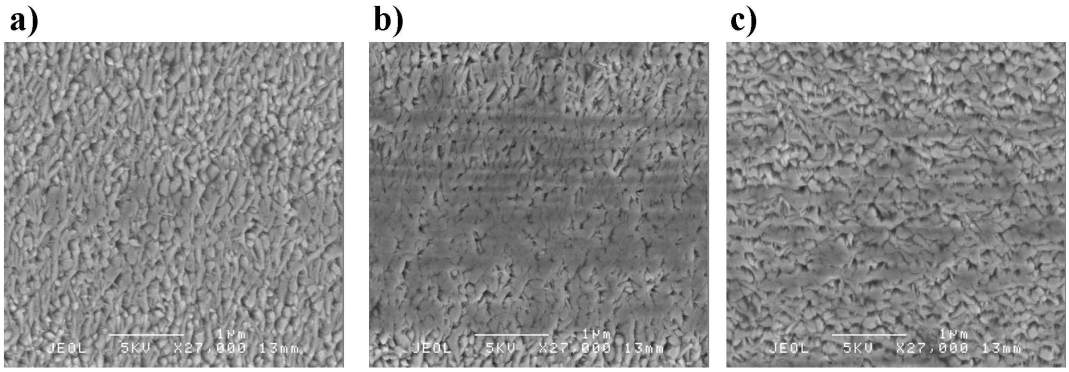

Figure 10: Typical SEM views of the friction track after sliding for three sputtering pressures : (a) 0.11 Pa , (b) 0.40 Pa and (c) 0.53 Pa and for the same incidence angle $\alpha = 75°$ (horizontal sliding direction)

to the target material. Due to enhanced collisions between sputtered particles and argon atoms, flux of chromium atoms impinging on the growing film becomes less directional [60]. The angular distribution of sputtered chromium incoming from the target surface is spread leading to a more randomized flux rather than pure ballistic and consequently, a saturation of the column angle β (cf. § 3.6).

3.2. Tribological properties of GLAD thin films in gross slip regime

3.2.1. Evolution of the average dynamic friction coefficient with the sputtering parameters

In contrast to what was previously observed by Abreu *et al* [21] and Lintymer *et al* [34] on chromium GLAD films in micro- and macrotribological tests, respectively, the initial columnar structure is not damaged after sliding using a multi-asperity nanotribometer (Fig. 10). So, the adhesion and the cohesion of these films are strong enough to sustain the contact solicitations - 150 MPa - whatever the coating conditions.

Fig. 11 shows the evolution of the average dynamic friction coefficient ($\overline{\mu_d}$) *vs.* the incidence angle α for the different argon sputtering pressures. For the lowest pressure (0.11 Pa), $\overline{\mu_d}$ abruptly increases when the incidence angle is higher than 50°. In constrast for the highest argon pressure (0.53 Pa), $\overline{\mu_d}$ displays a minimum for incidence angles in-between 20 and 40° revealing a bowl shape around these values. For the medium sputtering pressure (0.40 Pa), $\overline{\mu_d}$ shows two maxima (about 0.32) for 20° and 55° respectively, which reveal some kind of *local* effects probably induced by fine variations of the structure. As an unexpected

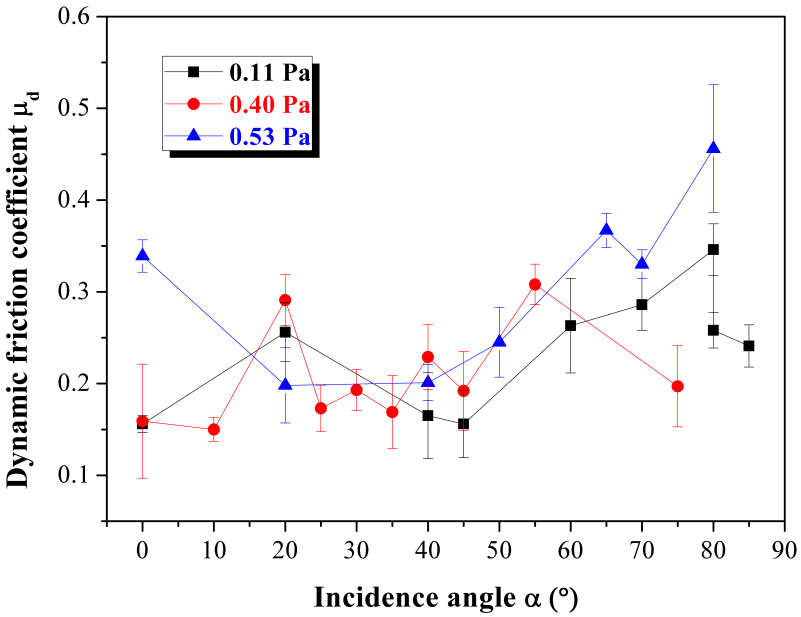

Figure 11: Variations of the average dynamic friction coefficient *vs.* incidence angle α for the three argon sputtering pressures

result, no difference is observed in the tribological behaviours carried out in the direction *"parallel"* and *"perpendicular"* to the orientation of the columns as reported by [23, 61]. However, these authors used a 17 µm radius diamond indenter tip as a slider - commonly used in nanoindentation test - which is probably more sensitive but also more destructive than ours (2 mm radius Si_3N_4 ball). In the same way, there is no real difference between tribological tests carried out *"with"* and *"against"* the tilt axis of the columns. This is probably due to the size of the contact area, which is much more important than both the columns size and the distance between the columns. Hence, the contact in multi-asperity nanotribology appears quite insensitive to the individual orientation of the columns. Indeed, as reported by many authors working on GLAD method [62, 63, 64], obtaining surface topographies without stochastic and non-separate surface features is the main challenge of this technique. However, a route to bypass this issue could be to create a seeded layer of known density and height prior to the GLAD deposition [27]. So, in our case, the column orientation β does not appear as the driving force that controls the change in the friction behaviour. But, referring to many authors [*eg.* 7], the films' density - and more particularly the films' porosity - are probably the main ones.

When the error bars appear to be low enough - as observed in Fig. 11 - a pseudo 3D-map - as shown in Fig. 12 - will be used instead of the classical 2D view in order to consider both the sputtering pressure and the incidence angle α (Fig. 12a) or the column angle β (Fig. 12b). Thus the comparision of Fig. 12 and Fig. 4 reveals that the increase of $\overline{\mu_d}$ starting from 45° and 55° (for 0.11 Pa and 0.53 Pa, respectively) strongly corresponds to the drop of the films' density down to 93%. In the same time, the minimun of $\overline{\mu_d}$ observed in-between 20° and 50° (Fig. 11 at 0.53 Pa) greatly corresponds to the zone where the film's density stays constant (Fig. 4). Thus, $\overline{\mu_d}$ appears as a parameter that is very sensitive to any change in the films' density as a bulk parameter.

However, in micro-gripping the static friction coefficient and more particularly the transition between the static and dynamic friction coefficient has probably a greater importance than the dynamic one only.

3.2.2. Evolution of the average static friction coefficient with the sputtering parameters

Fig. 13 shows the pseudo 3D-maps of the average static friction coefficient $\overline{\mu_s}$ computed from the whole of cycles (10 cycles back and forward). Overall, $\overline{\mu_s}$ has the same *global* behaviour than $\overline{\mu_d}$ with respect to the operating parameters. Nevertheless it definitely appears more sensitive than the latter to any *local*

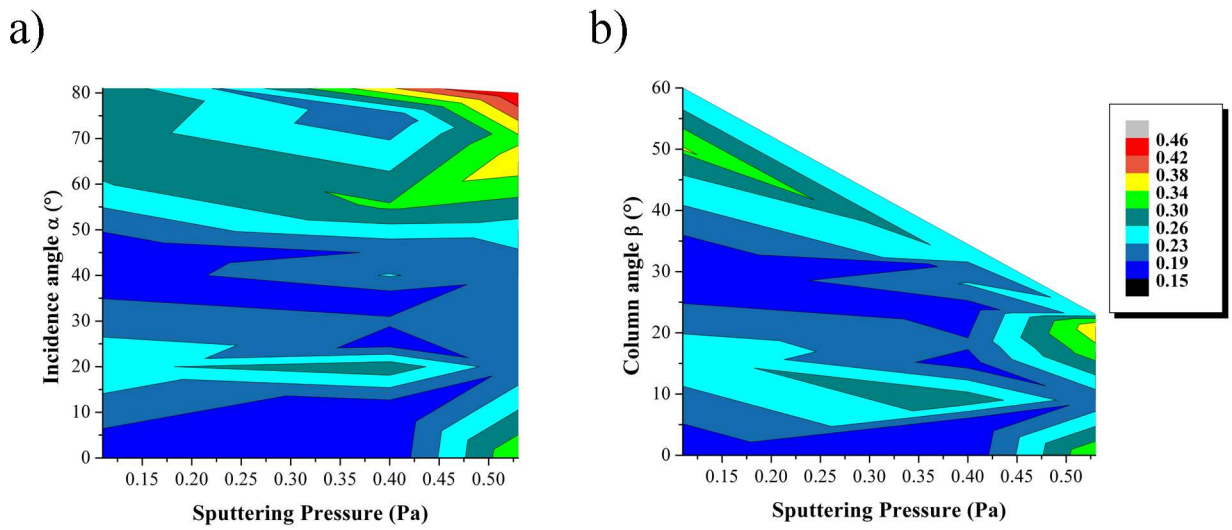

Figure 12: Pseudo 3D-maps displaying the evolution of the average dynamic friction coefficient μ_d as a function of the sputtering argon pressure and (a) the incidence angle α and (b) the column angle β

tribological variations linked to low variations in the sputtering parameters. Thus,

- for the lowest pressure (0.11 Pa), $\overline{\mu_s}$ is rather constant until $\alpha = 50°$ and strongly increases when the film's density drops as reported for $\overline{\mu_d}$;
- when the argon sputtering pressure increases from 0.11 to 0.53 Pa, there are column angles β (Fig. 13b) where $\overline{\mu_s}$ displays a maximum ($\overline{\mu_s} \simeq 0.5$ at 0.40 Pa) or a minimum ($\overline{\mu_s} \simeq 0.17$ at 0.53 Pa). Besides, around these latter, $\overline{\mu_s}$ can be strongly modified - *i.e* multiplied or divided by a factor 2 - when β is shifted to $\pm 5°$ (corresponding to a shift of α around 10° as shown in Fig. 13a).

Thus, for the lowest sputtering pressure, the behaviour of the static friction coefficient is the same as the dynamic one - *i.e* controlled by the films's density as a bulk property. But, for a given sputtering pressure higher than 0.11 Pa - corresponding to a change in the sputtering mechanism from a pure ballistic to a more randomised one (cf. § 3.1) - the static friction coefficient can accurately be controlled by adjustement of the incidence angle α. Since the dynamic friction coefficient is less sensitive than the static one, it is also possible to adjust the ratio $\frac{\overline{\mu_s}}{\overline{\mu_d}}$ by tuning $\overline{\mu_s}$ that allows to accurately control the transition from sticking to sliding by avoiding the stick-slip occurrence [65] and its consequences on the friction [66] and wear behaviours [67]. For example, Fig. 14 shows two different cases where the stick-slip occurence is completely avoided when $\overline{\mu_s} = \overline{\mu_d}$ (at 0.40 Pa and $\alpha = 5°$ or $\alpha = 35°$) or when the sticking is favoured over the slipping when $\overline{\mu_s} \gg \overline{\mu_d}$ (*e.g.* $\overline{\mu_s} > 2.\overline{\mu_d}$ at 0.40 Pa and $\alpha = 45°$ or $\alpha = 75°$). Hence, tuneable tribological properties can easily be obtained in micro-gripping by using suitable sputtering operating parameters.

However, in constrast to what is observed for $\overline{\mu_d}$ (Fig. 4 and 12), the evolution of $\overline{\mu_s}$ with the operating parameters can not be directly explained by considering the films' density only. Indeed, Fig. 13a is not directly comparable with Fig. 4 as reported for $\overline{\mu_d}$. So, it is necessary to remind the physical origins of the static coefficient according to the literature: $\overline{\mu_s}$ originates from the *static* real contact area controlled by the physico-chemical properties of the surfaces, in contrast to $\overline{\mu_d}$, which is mainly governed by the mechanical properties at the scale of the micro-asperities including elasticity, stiffness and inertia of the contact [18]. In order to understand the relationship between the static coefficient behaviour and the operating parameters, the physico-chemical and mechanical properties of GLAD films will be studied successively using (i) *wettability* [15, 18, 38] and *fractal dimension* assessment [36, 37, 45, 47, 48, 68, 69, 70] on the one hand, and (ii) *lateral contact stiffness* measurement on the other hand [56].

3.3. Wettability - Evolution of the contact angle of a water drop with the sputtering parameters

Fig. 15 shows the variations of the contact angle θ of a water drop as a function of the incidence angle α for the three sputtering pressures. It appears that the nanostructured surfaces are mainly *hydrophobic*

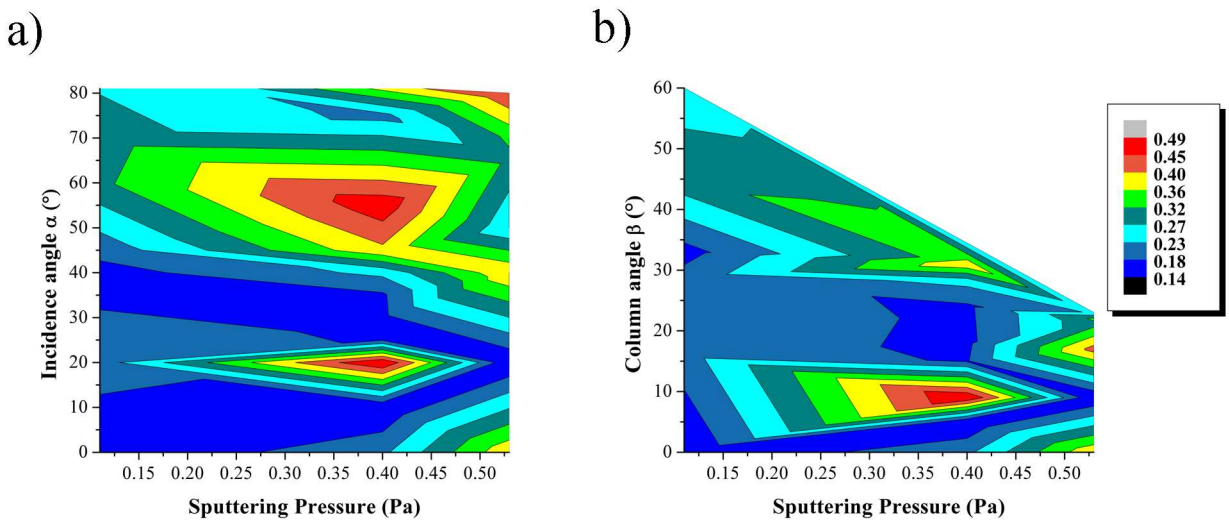

Figure 13: Pseudo 3D-maps displaying the evolution of the average static friction coefficient μ_s as a function of the sputtering argon pressure and (a) the incidence angle α and (b) the column angle β

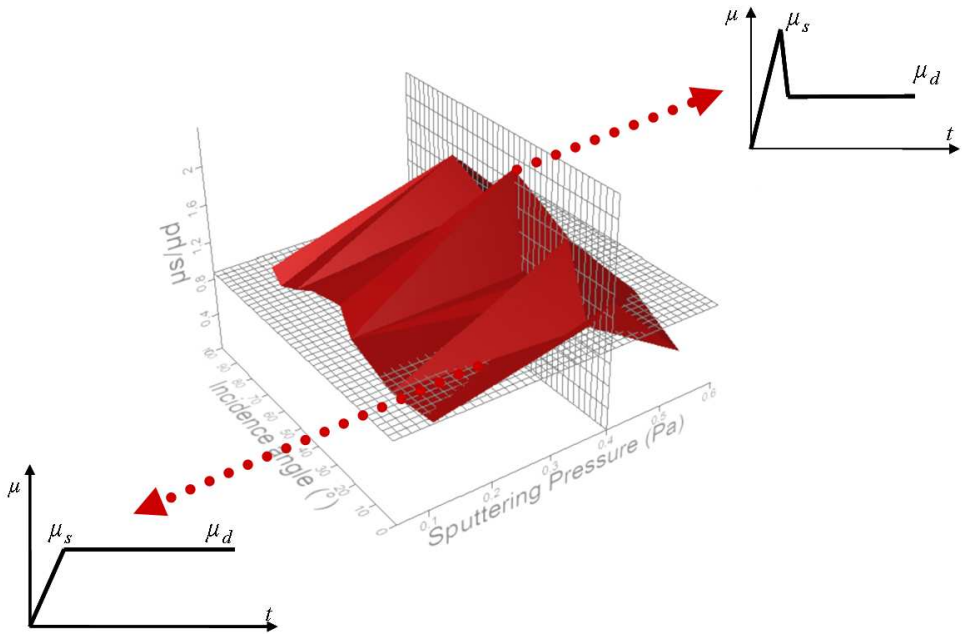

Figure 14: 3D-map displaying the evolution of the ratio $\frac{\overline{\mu_s}}{\overline{\mu_d}}$ as a function of the sputtering argon pressure and the incidence angle α. This map is very useful to predict the operating parameters (i) to avoid any stick-slip phenomenon - *e.g.* when $\overline{\mu}_s = \overline{\mu}_d$ for 0.40 Pa, $\alpha = 35°$ - or on the contrary, (ii) to favour sticking over slipping when $\overline{\mu_s} \gg \overline{\mu_d}$ (*e.g.* 0.40 Pa, $\alpha = 75°$ when $\overline{\mu_s} > 2.\overline{\mu_d}$)

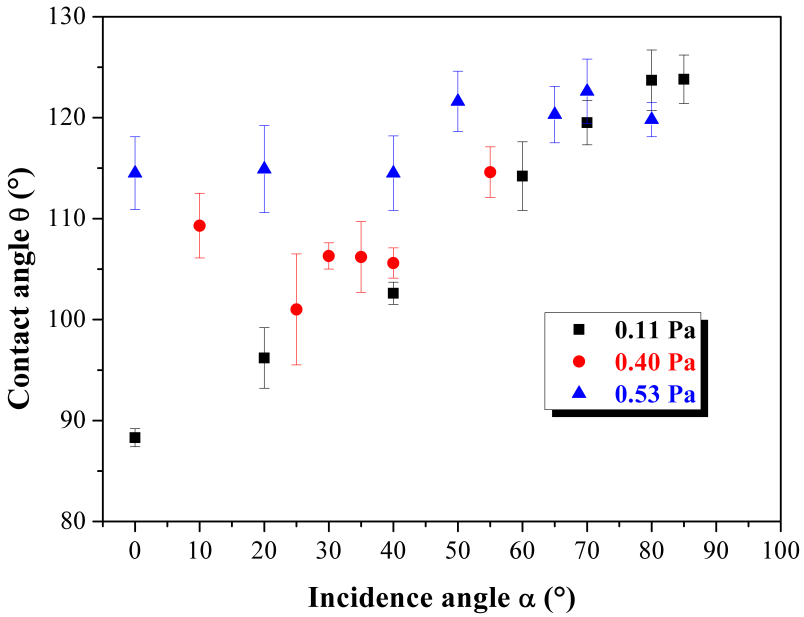

Figure 15: Variation of the contact angle θ of a water drop *vs.* incidence angle α for the three sputtering pressures

($\theta > 90°$) in contrast to the initial chromium target, which is *hydrophilic* ($\theta = 49.1° \pm 0.6$). Thus, the contact angle θ of a water drop - and consequently the underlying adhesive contribution of friction due to the capillary effects - seems to be controlled by the nanostructuration of the surfaces [7, 71, 72]. In our case, the contact angle of the water drop clearly depends on the sputtering pressure:

- for the highest pressures (0.53 Pa) the contact angle is rather constant (about 117°) ;
- in contrast for the lowest pressure (0.11 Pa), the contact angle continuously increases from a *hydrophilic* behaviour to a *hydrophobic* one. A linear trend is even noticed with a good correlation coefficient (r = 0.99) revealing an enhancement of the *hydrophobic* behaviour with the incidence angle α. However, the contact angle does not evolve anymore for the highest incidence angles. This result is in good agreement with the theories proposed successively by Wenzel (1936) and Cassie-Baxter (1944) in order to explain the wettability of heterogeneous surfaces [7, 9, 10, 71, 72]. This saturation value (around 125°) is probably due to the shadowing effect at the atomic scale as mentioned in § 2.2.1.

As reported in Fig. 16, the evolution of the water drop contact angle θ as a function of the operating parameters reveals that the wettability varies as well as the films' density (Fig. 4) leading to the conclusion that the variations of the contact angle θ is directly controlled by the films' porosity - described as air pockets, which are able to control the water droplet spreading out [7].

However, the size of the water drop being greatly larger than the *static* real contact area, the variations of the contact angle θ as a function of the film's density are not really accurate enough to explain that of $\overline{\mu_s}$. Hence, an accurate experimental assessement of the coatings' density is needed. The *fractal dimension* is one of them because it provides accurate informations about the degree of fragmentation of the surfaces.

3.4. Evolution of the fractal dimension with the sputtering parameters

For thin coatings, the fragmentation of the surfaces is strongly connected to the degree of porosity of these ones: the more the surface is fragmented, the higher is the *fractal dimension* (D_f in-between 2 and 3). Thus, as wettability, *fractal dimension* should be representative of the film's porosity but with a greater sharpness due to the topographic assessment technique - *i.e* AFM and interferometric profilometry - more accurate than the water drop one.

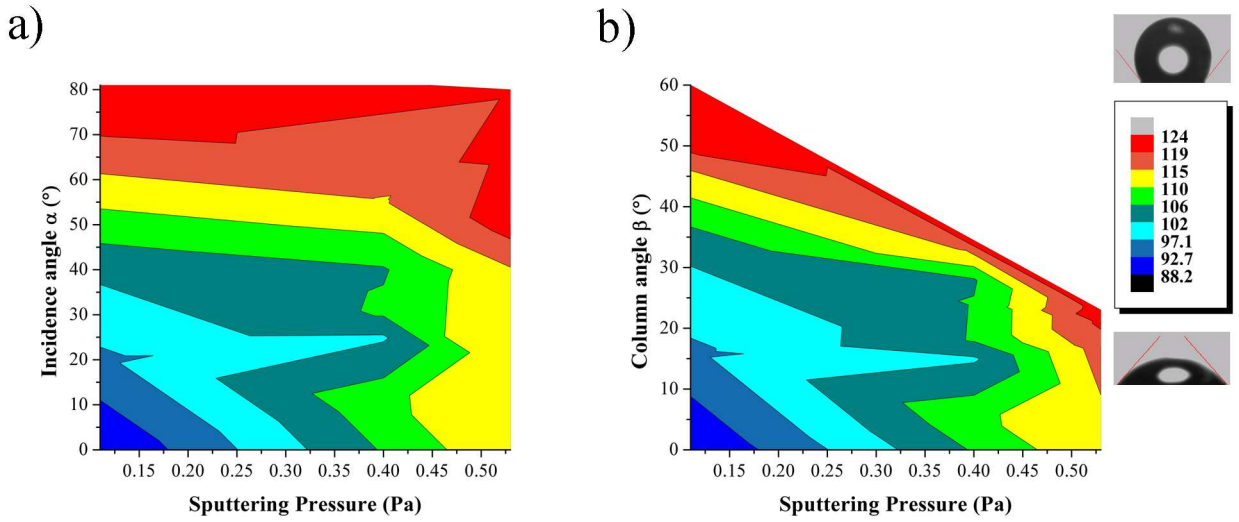

Figure 16: Pseudo 3D-maps displaying the evolution of the average contact angle θ of a water drop (in °) as a function of the sputtering argon pressure and (a) the incidence angle α and (b) the column angle β

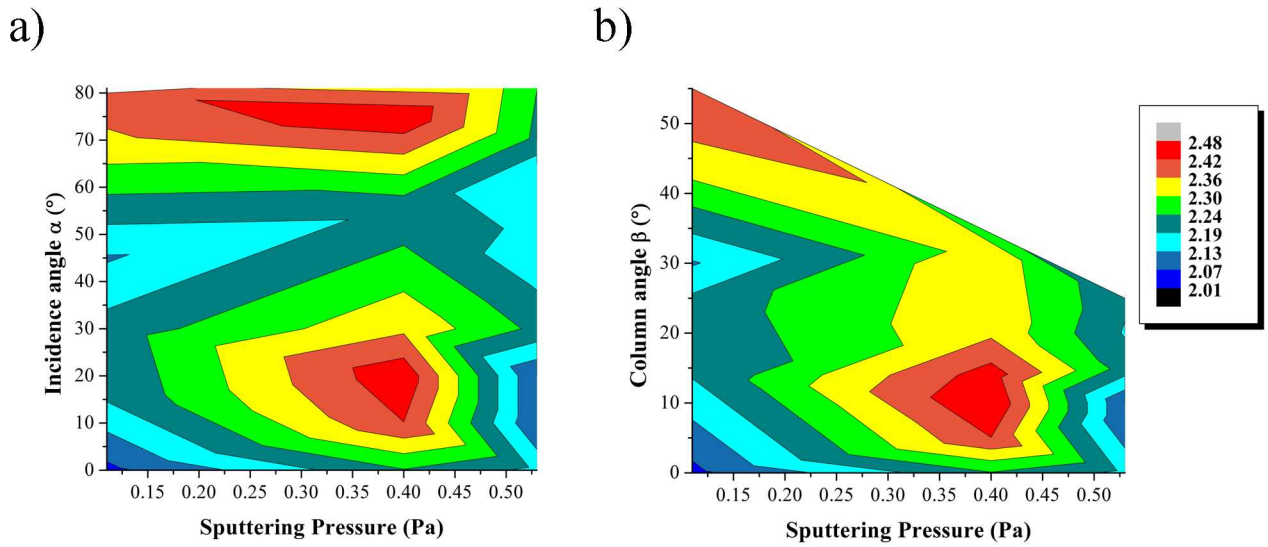

Figure 17: Pseudo 3D-maps displaying the evolution of the average fractal dimension $\overline{D}_f$ as a function of the sputtering argon pressure and (a) the incidence angle α and (b) the column angle β

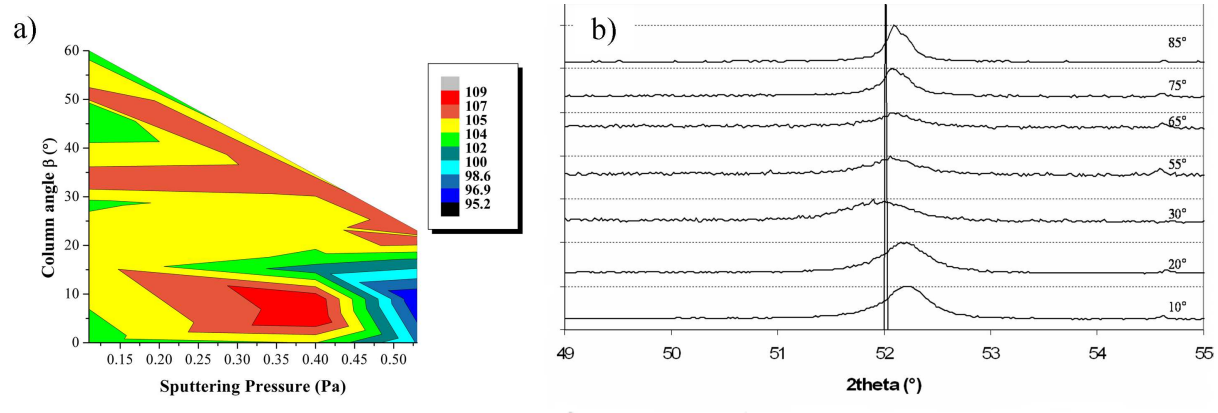

Figure 18: a) Pseudo 3D-map displaying the evolution of the average *lateral contact stiffness* (Nm^{-1}) as a function of the sputtering argon pressure and for various column angles β and b) X-ray diffraction patterns of chromium thin films deposited at 0.40 Pa and for various incidence angles α (the sharp central peak is the chromium one corresponding to the initial target)

As expected, in first approximation and in great agreement with the literature [68, 69, 70], Fig. 17 reveals that $\overline{D}_f$ varies as the wettability results. In the same way, there is no obvious correlation between $\overline{\mu_d}$ (Fig. 12) and $\overline{D}_f$ in agreement with Ganti *et al* [47]. However, as an unexpected result, it appears that $\overline{D}_f$ has the same variations as $\overline{\mu_s}$ (Fig. 13): especially the positions of their maximum (at 0.40 Pa and $\alpha = 20°$) and minimum (at 0.53 Pa and $\alpha = 20°$) are quite similar. Thus, the variations of $\overline{\mu_s}$ seem strongly correlated with that of $\overline{D}_f$, which appears as the *local* variations of the films' porosity - shown as air pockets. Besides, the fractal dimension's map (Fig. 17) gives more accurate informations about the surface than those computed from a theoretical model (Fig. 4), which can not take into account the *local* variations of the real nanostructures. It is well known [71], that the latter - by means of secondary grain growth for instance - is able to create some kind of instabilities at the scale of the micro-nanocontact due to capillary effects. Thus, the *local* variations of $\overline{\mu}_s$ could be explained by considering the *local* variations of the films' porosity - *i.e* at the scale of the columns - revealed by the *local* variations of the fractal dimension $\overline{D}_f$. However, these ones could also locally change the mechanical properties of the surfaces and consequently the friction behaviour too. These evolutions can be assessed by means of the *lateral contact stiffness* (k_L).

3.5. Evolution of the lateral contact stiffness with the sputtering parameters

As mentioned before (§ 2.3), the *lateral contact stiffness* (k_L) is the slope from the friction force *vs.* lateral displacement when the oscillation amplitude is lower than the contact radius (± 10 µm) - *i.e* when the thin film is submitted to an alternative shear testing where no sliding occurs. Referring to Mindlin *et al.* [56], this *lateral contact stiffness* $k_L(Nm^{-1})$ is connected to the elastic properties of samples as follow:

$$k_L = 8a\frac{1}{\frac{2-\nu_1}{G_1} + \frac{2-\nu_2}{G_2}} \tag{2}$$

where a is the contact radius (m), G_i and ν_i are the shear modulus (Nm^{-2}) and the Poisson'ratio of each sample, respectively.

Fig. 18a reveals that the variations of the average *lateral contact stiffness* $\overline{k}_L$ are quite low (from 95 to 109 Nm^{-1}) because the surface is rather homogeneous and dense enough in the thickness to insure the mechanical cohesion of the films (the average value is about 103 Nm^{-1}). These results are in good agreement with the XRD ones, which reveal similar diffraction patterns with respect to the operating parameters. Hence, $\overline{k}_L$ - and consequently the elastic properties of the films - is not really controlled by the sputtering operating parameters.

However some variations of $\overline{k}_L$ - similar to that of $\overline{D}_f$ and $\overline{\mu_s}$ - are locally observed: thus, as shown in Fig. 18a, the maximum of the *lateral contact stiffness* clearly corresponds to the maximum of $\overline{\mu_s}$ (Fig. 13b) but elsewhere the variations of $\overline{k}_L$ can not be directly connected to the variations of $\overline{\mu_s}$. These results are also in good agreement with the XRD ones (Fig. 18b), which reveal both a widening and a shift of the (110) peak with an incidence angle α in-between 30 and 50°. This peaks behaviour is typical of either (i)

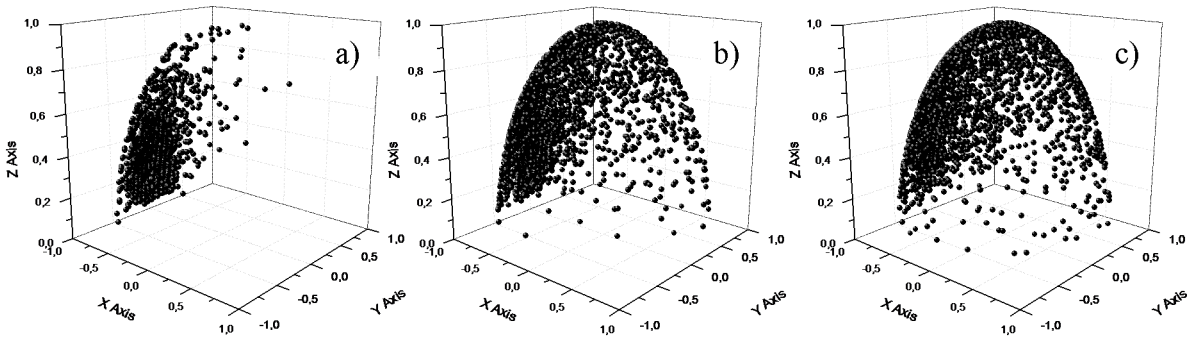

Figure 19: Angular distribution of chromium sputtered particles obtained from SIMTRA [73] for an incidence angle $\alpha = 80°$ and for an argon sputtering pressure of a) 0.11 Pa; b) 0.40 Pa; c) 0.53 Pa.

some changes of the crystallites size or (ii) the presence of potential tension micro-stresses within the films fabricated at 0.40 Pa with these incidence angles. Thus, the *global* variations of the films' porosity do not really change the mechanical properties of the films: the latter are quite homogeneous and controlled by the denser subsurface. However, the *local* variations of the *lateral contact stiffness* - which are the same as those of $\overline{D_f}$ and $\overline{\mu_s}$ - could be correlated with either (i) the presence of internal stresses or (ii) some changes of the crystallites size as reported before by the secondary grain growth. So, there is clearly a relation between growth, structure and tribological properties.

3.6. Relation between growth, structure and tribological properties

For the lowest sputtering pressure (0.11 Pa), chromium thin films exhibit a regular columnar structure. As previously observed in Fig. 9, growing of the highest column angle β is produced for a systematic rise of the incidence angle α. In addition, the columnar structure is kept for high sputtering pressures but, β angle saturates at 35 and 22° for the corresponding pressure of 0.40 and 0.53 Pa, respectively. Such regular columnar growth observed at 0.11 Pa is mainly attributed to the directional flux of the sputtered particles, which is especially favoured at low sputtering pressure (Fig. 19).

Simulation of the particles flux from *SIMTRA software* [73] allows the determination of the sputtered particles trajectories taking into account the geometry of the sputtering chamber and operating conditions (*e.g.* pressure, ion current density on the target, ...). It is worth of noting that this spatial distribution exhibit a strong directional flux at 0.11 Pa and for an incidence angle $\alpha = 80°$ (Fig. 19a). An increasing sputtering pressure up to 0.40 Pa leads to a spreading of the distribution (Fig. 19b), which is even more emphasized at 0.53 Pa (Fig. 19c). As a result, such a loss of the directional particles flux with the sputtering pressure has to be correlated with some features of the columnar growth as well as some singularities of the *static friction coefficient*, the *fractal dimension* and to some extents the *lateral contact stiffness*.

- On the one hand, for sputtering pressure of 0.11 Pa, the evolution of the columnar orientation *vs.* incidence angle α is smooth. A regular growth is produced due to a narrow spatial distribution of the particles flux (Fig. 19a). So, most of the sputtered atoms impinge on the growing film according to the given incidence angle α. Thus, a gradual variation of the tribological properties (Fig. 11), water drop contact angle θ (Fig. 15), fractal dimension (Fig. 17) are measured as a function of the incidence angle α. As a result, variations of $\overline{\mu_s}$ are quite similar to the $\overline{\mu_d}$ ones.

- On the other hand, an increasing sputtering pressure does not solely reduce the mean free path of the sputtered atoms and so, the scattering of the flux. It also favours the secondary grain growth in thin films, as illustrated in Fig. 20 for chromium thin films exhibiting a spiral columnar structure. Thus, a multi-directional character of the particles flux prevails against a single oriented flux for the chosen incidence angle $\alpha = 80°$. Thermalization effect of the sputtered particles occurs and gives rise to a more randomized growth of the columnar structure leading to *local* variations of surfaces properties as porosity as recently reported [31]. Tribological behaviours of the films prepared at high pressure can be closely linked to this secondary grain growth because of the loss of the directional feature of the

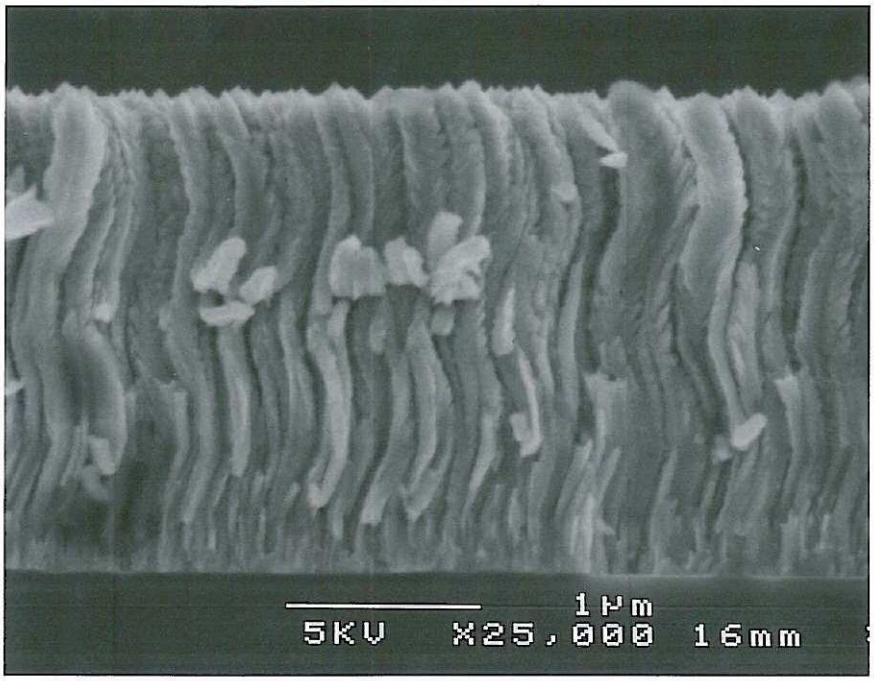

Figure 20: Chromium thin films sputter-deposited at a sputtering pressure of 0.53 Pa. A spiral growth of the columns is obtained using a constant incidence angle $\alpha = 80°$ and a substrate rotation $\phi = 0.5$ revolution per hour. A secondary grain growth can be clearly observed.

sputtered particles. Typical *local* variations of static friction coefficient, the highest fractal dimension or the strongest lateral contact stiffness are systematically observed for incidence angles $\alpha = 0$ to 30° (corresponding β angles are 0 to 20°) and for pressures in-between 0.30 to 0.50 Pa. Therefore, this range of incidence angles and pressures well correlate with changes of the nanostructure due to secondary grain growth, and friction behaviours. Hence, this range of sputtering pressures enables to tailor tribological properties favouring sticking over sliding or, in contrast, avoiding any stick-slip occurrence.

4. Conclusion

In this work, chromium thin films were sputter deposited implementing the GLancing Angle Deposition (GLAD) method (*i.e* the incident vapour flux strikes onto the substrate at tilted angles α) in order to create inclined nanosculptured thin films for controlling tribological behaviour in micro-gripping applications. Three sputtering pressures 0.11, 0.40 and 0.53 Pa were used and the incidence angle α of the sputtered particles was systematically changed from 0 to 80°. Firstly, results reveal that the mechanical properties of the films - as a bulk parameters - do not really change with the sputtering parameters. Secondly, tribological behaviour - including surface properties - is strongly correlated with the growth mechanism and the structure of the films, which are both linked with the operating sputtering parameters. Thus,

- for the lowest sputtering pressures, a regular growth is produced due to a narrow spatial distribution of the particles flux. So, chromium films exhibit a regular columnar structure. The variation of the column orientation is very smooth with the incidence angle α. A gradual variation of the tribological properties, and especially the wettability is noticed as a function of the incidence angle α. In practice, this level of sputtering pressure is quite interesting for tailoring surfaces displaying a gradient of wettability ;
- in contrast, when the sputtering pressures are increased beyond the pure balistic sputtering area, the mean free path of the sputtered atoms is strongly reduced, and so the scattering of the flux prevails. In addition, secondary grain growth in the thin films generally occurs. Thus a multi-directional character

of the particles flux is enhanced against a single oriented flux leading to a more randomized growth of the columnar structure. Local variations of static friction coefficient, wettability, surface porosity and lateral contact stiffness are typically observed in this range of sputtering pressures. This latter enables to tailor suitable surfaces properties by tuning the incidence angle α favouring sticking over sliding or, in contrast, avoiding any stick-slip occurrence. Indeed, the static friction - and more particularly the ratio $\frac{\mu_s}{\mu_d}$ - can easily be adjusted to control the transition from sticking to sliding in micro-gripping.

Acknowledgments

The authors are grateful to the *Région Franche Comté* (France) for its financial support under the awards *FIMICAP : Reliability of microscale assembly and design of smart sensors using surface engineering.*

References

[1] P. Lambert, Capillary Forces in Microassembly, Springer, ISBN 978-0-387-71088-4, 2007.

[2] K. Goser, P. Glösekötter, J. Dienstuhl, Nanoelectronics and Nanosystems, Springer Berlin Heidelberg, ISBN 3-540-40443-0, 2004.

[3] E. Gnecco, E. Meyer, Fundamentals of friction and wear on the nanoscale, Springer Berlin Heidelberg, ISBN 978-3-540-36806-9, 2007.

[4] T. Pradeep, NANO: The Essentials - Understanding Nanoscience & Nanotechnology, Mc Graw Hill, ISBN 978-0-07-154829-8, 2008.

[5] T.-R. Hsu, MEMS & Microsystems, Wiley, 2nd edn., ISBN 978-0-470-08301-7, 2008.

[6] M. Gauthier, S. Regnier, P. Rougeot, N. Chaillet, Forces analysis for micromanipulation in dry and liquid environments, J. Micromechatronics 3 (2006) 389–413;.

[7] M. Nosonovsky, B. Bhushan, Multiscale Dissipative Mechanisms and Hierarchical Surfaces, Springer Berlin Heidelberg New York, ISBN 978-3-540-78424-1, 2008.

[8] M. Nosonovsky, B. Bhushan, Multiscale friction mechanisms and hierarchical surfaces in nano- and bio-tribology, Materials Science and Engineering R 58 (2007) 162–193.

[9] M. Nosonovsky, B. Bhushan, Hierarchical roughness optimization for biomimetic superhydrophobic surfaces, Ultramicroscopy 107 (2007) 969–979.

[10] B. Bhushan, Y. Jung, Natural and biomimetic artificial surfaces for superhydrophobicity, self-cleaning, low adhesion, and drag reduction, Progress in Materials Science (56) (2011) 1–108.

[11] D. Marchetto, A. Rota, L. Calabri, G. Gazzadi, C. Menozzi, S. Valeri, Hydrophobic effect of surface patterning on Si surface, Wear 268 (2010) 488–492.

[12] D. Marchetto, A. Rota, L. Calabri, G. Gazzadi, C. Menozzi, S. Valeri, AFM investigation of tribological properties of nano-patterned silicon surface, Wear 265 (2008) 577–582.

[13] C. Yang, U. Tartaglino, B. Persson, Influence of surface roughness on superhydrophobicity, Phys. Rev. Letters 97 (2006) 116103.

[14] F. Borodich, B. Galanov, S. Grob, Y. Prostov, Adhesive contact problems at macro and nanoscales, in: F. Franek, W. Bartz (Eds.), Proceedings of the 3rd European Conference on Tribology, June 7-9, 2011, Vienna, Austria, 15–20, 2011.

[15] C. Mate, Tribology on the small scale, NY: Oxford University Press, ISBN 978-0-19-852678-0, 2008.

[16] B. Persson, O. Albohr, U. Tartaglino, A. Volokitin, E. Tosatti, On the nature of surface roughness with application to contact mechanics, sealing, rubber friction and adhesion, J. Phys.: Condens. Matter 17 (2005) R1–R62.

[17] D. Maugis, Contact, Adhesion and Rupture of Elastic Solids, Springer Berlin Heidelberg, ISBN 978-3540661139, 2000.

[18] B. Persson, Sliding Friction - Physical principles and application, Springer Berlin Heidelberg New York, 2nd edn., ISBN 3-540-67192-7, 2000.

[19] A. Casoli, M. Brendlé, J. Schultz, P. Auroy, G. Reiter, Friction Induced by Grafted Polymeric Chains, Langmuir 17 (2001) 388–398.

[20] J. Takadoum, Materials Science & Engineering in Tribology, Wiley, ISTE Ltd, ISBN 978-1-84821-067-7, 2008.

[21] C. Abreu, N. Martin, J. Gomes, Chromium sculptured thin films: tribological evaluation under macro- and micro-testing conditions, in: Proceedings of the NordTrib 2010, paper 35, 2010.

[22] A. Lakhtakia, R. Messier, Sculptured Thin Films, Nanoengineerred Morphology and Optics, SPIE Press, Bellingham, Washington USA, ISBN 081945606-3, 2005.

[23] E. So, M. Demirel, K. Wahl, Mechanical anisotropy of nanostructured parylene films during sliding contact, J. Phys. D: Appl. Phys. 43 (2010) 045403.

[24] N. Young, J. Koval, Optically active fluorite films, Nature 183 (1959) 104.

[25] K. Robbie, J. Sit, M. Brett, Advanced techniques for glancing angle deposition, J. Vac. Sci. Technol. B16 (1998) 1115.

[26] K. Robbie, M. Brett, A. Lakhtakia, Chiral sculptured thin films, Nature 384 (1999) 384.

[27] A. Dolatshahi-Pirouz, D. Sutherland, M. Foss, F. Besenbacher, Growth characteristics of inclined columns produced bt Glancing Angle Deposition (GLAD) and colloidal lithography, Appl. Surf. Sci. 257 (2011) 2226.

[28] J. Lintymer, J. Gavoille, N. Martin, J. Takadoum, Microstructure and properties of sputter deposited chromium thin films, Surface & Coatings Technology 174-175 (2003) 316.

[29] C. Zhou, D. Gall, The structure of Ta nanopillars grown by glancing angle deposition, Thin Solid Films 515 (2006) 1223–1227.

[30] C. Gaire, D.-X. Ye, F. Tang, R. Picu, G.-C. Wang., T.-M. Lu, Mechanical Testing of Isolated Amorphous Silicon Slanted Nanorods, Journal of Nanoscience and Nanotechnology 5 (2005) 1893–1897.

[31] Y. Yang, D. Hass, H. Wadley, Porosity control in zig-zag vapor-deposited films, Thin Solid Films 471 (2005) 1–11.

[32] D.-L. Liu, D.-X. Ye, F. Khan, F. Tang, B.-K. Lim, R. Picu, G.-C. Wang., T.-M. Lu, Mechanics of Patterned Helical Si Springs on Si Substrate, Journal of Nanoscience and Nanotechnology 3 (6) (2003) 492–495.

[33] A. Besnard, Relation structure-conductivité électrique dans les films de chrome architecturés, Ph.D. thesis, Université de Franche Comté, 2010.

[34] J. Lintymer, Etude de l'influence de la microstructure sur les propriétés mécaniques et électriques de couches de chrome en zigzag élaborées par pulvérisation cathodique, Ph.D. thesis, Université de Franche-Comté, 2003.

[35] A. Besnard, N. Martin, L. Carpentier, B. Gallas, A theoretical model for the electrical properties of chromium thin films sputter deposited at oblique incidence, J. Phys. D: Appl. Phys. 44 (2011) 215031.

[36] M. Khadar, N. Shanid, Nanoscale fine-structure evaluation of RF magnetron sputtered anatase films using HRTEM, AFM, micro-Raman spectroscopy and fractal analysis, Surface & Coatings Technology 204 (2010) 1366–1374.

[37] C. Douketis, Z. Wang, T. Haslett, M. Moskovits, Fractal character of cold-deposited silver films determined by low-temperature scanning tunneling microscopy, Phys. Rev. B 51 (16) (1995) 51.

[38] B. Bhushan, Nanotribology and Nanomechanics, an introduction, Springer Berlin Heidelberg, ISBN 3-540-24267-8, 2005.

[39] K. Harris, D. Vick, E. Gonzalez, T. Smy, K. Robbie, M. Brett, Porous thin films for thermal barrier coatings, Surface & Coatings Technology 138 (2001) 185.

[40] M. Colgan, M. Brett, Field emission from carbon and silicon films with pillar microstructure, Thin Solid Films 389 (2001) 1.

[41] B. Dick, M. Brett, T. Smy, M. Freeman, M. Malac, R. Egerton, Periodic magnetic microstructures by glancing angle deposition, J. Vac. Sci. Technol. A18 (2000) 1838.

[42] M.Gauthier, S.Regnier, (Editors), Robotic Micro-Assembly, Wiley-IEEE Press, 2010, ISBN: 978-0-470-48417-3.

[43] N. Chaillet, S.Regnier, Microrobotics for Micromanipulation, STE Ltd and John Wiley & Sons Inc, 2010, ISBN-10: 1848211864, ISBN-13: 978-1848211865.

[44] S. Paik, S. Kim, I. Schuller, R. Ramirez, Surface kinectics and roughness on microstructure formation in thin films, Phys. Rev. B43 (2) (1991) 1843.

[45] D. Raoufi, Fractal analyses of ITO thin films: A study based on power spectral density, Physica B 405 (2010) 451–455.

[46] B. Mandelbrot, Fractals: form, chance and dimension, Freeman, San Francisco, ISBN 978-2-0812-4617-1, 1984.

[47] S. Ganti, B. Bhushan, Generalized fractal analysis and its applications to engineering surfaces, Wear 180 (1995) 17–34.

[48] J.-J. Gagnepain, C. Roques-Carmes, Fractal approach to two-dimensional and three-dimensional surface roughness, Wear 109 (1986) 119–126.

[49] W. Zahn, A. Zösch, The dependance of fractal dimension on measuring conditions of scanning probe microscopy, Fresenius J Analen Chem 365 (1999) 168–172.

[50] A. van Put, A. Vertes, D. Wegrzynek, B. Treiger, R. van Grieken, Quantitative characterization of individual particle surfaces by fractal analysis of scanning electron microscope images, Fresenius J Analen Chem 350 (1994) 440–447.

[51] A. Mannelquist, N. Almquist, S. Fredriksson, Influence of tip geometry on fractal analysis of atomic force microscopy images, Appl. Phys. A 66 (1998) 891–895.

[52] A. Czifra, I. Baranyi, G. Kalacska, Fractal analysis of microtopographies in wear, in: F. Franek, W. Bartz (Eds.), Proceedings of the 3rd European Conference on Tribology, June 7-9, 2011, Vienna, Austria, 593–596, 2011.

[53] W. Zahn, Characterization of thin film surfaces by fractal geometry, Fresenius J Analen Chem 358 (1997) 119–121.

[54] T. Thomas, Rough Surfaces, Imperial College Press, 2nd ed. edn., ISBN 978-1860941009, 1999.

[55] P. Stempflé, J. Takadoum, Multi-asperity nanotribological behavior of single-crystal silicon: Crystallography-induced anisotropy in friction and wear, Tribology International 48 (2012) 35–43.

[56] R. Mindlin, W. Mason, J. Osmer, H. Deresiewicz, Effects of an oscillating tangential force on the contact surfaces of elastic spheres, Proc. 1st US National Congress of Applied Mechanics ASME [227] (1952) 203.

[57] J. Thornton, Influence of apparatus geometry and deposition conditions on the structure and topography of thick sputtered coatings, J. Vac. Sci. Technol. 11 (1974) 666.

[58] J. Nieuwenhuizen, H. Haanstra, Microfractography of thin films, Philips Tech. Rev. 27 (1966) 87.

[59] Y. Yamamura, K. Muraoka, Overcosine angular distribution of sputtered atoms at normal incidence, Nucl. Instrum. Methods B42 (1989) 175.

[60] H. Fujiwara, K. Hara, M. Kamiya, T. Hashimoto, K. Okamoto, Comment on the tangent rule, Thin Solid Films 163 (1998) 387.

[61] H. Hirakata, T. Nishihira, A. Yonezu, K. K. Minoshima, Frictional Anisotropy of Oblique Nanocolumn Arrays Grown by Glancing Angle Deposition, Tribology Letters 44 (2011) 259–268.

[62] K. Robbie, M. Brett, Sculptured thin films and glancing angle deposition: Growth mechanics and applications, J. Vac. Sci. Technol. A15 (1997) 1460.

[63] A. Dolatshahi-Pirouz, C. Pennisi, S. Skeldal, M. Foss, J. Chevallier, V. Zacher, P. Andreasen, K. Yoshida, F. Besenbacher, The influence of glancing angle deposited nano-rough platinum surfaces on the adsorption of fibrinogen and the proliferation of primary human fibroblasts, Nanotechnology 20 (2009) 095101.

[64] A. Dolatshahi-Pirouz, M. Hovgaard, K. Rechendorff, J. Chevallier, M. Foss, F. Besenbacher, Scaling behavior of the surface roughness of platinum films grown by oblique angle deposition, Phys. Rev. B 77 (2008) 115427.

[65] F. Heslot, T. Baumberger, B. Perrin, B. Caroli, C. Caroli, creep, stick-slip, and dry-friction dynamics: experiments and a heuristic model, Phys. Rev. E 49 (1994) 4973–4988.

[66] M. Scherge, J. Schaefer, Microtribological investigations of stick/slip phenomena using a novel oscillatory friction and adhesion tester, Tribology Letters 4 (1998) 37–42.

[67] M. Brendlé, P. Diss, P. Stempflé, Nanoparticle detachment: a possible link between macro and nanotribology?, Tribology Letters 9 (2000) 97–104.

[68] F. Bottiglione, G. Carbone, Super-hydrophobicity of fractal surfaces, in: F. Franek, W. Bartz (Eds.), Proceedings of the 3rd European Conference on Tribology, June 7-9, 2011, Vienna, Austria, 267–271, 2011.

[69] T. Onda, S. Shibuichi, N. Satoh, K. Tsujii, Super-water-Repellent fractal surfaces, Langmuir 12 (9) (1996) 2125–2127.

[70] S. Sarkar, S. Patra, N. Gayathri, S. Banerjee, Effect of self-affine fractal characteristics of surfaces on wetting, Appl. Phys. Letters 96 (2010) 063112.

[71] M. Nosonovsky, B. Bhushan, Capillary effects and instabilities in nanocontacts, Ultramicroscopy 108 (2008) 1181–1185.

[72] S. Cai, B. Bhushan, Meniscus and viscous forces during separation of hydrophilic and hydrophobic surfaces with liquid-mediated contacts, Materials Science and Engineering R 61 (2008) 78–106.

[73] K. van Aeken, S. Mahieu, D. Depla, The metal flux from a rotating cylindrical magnetron: a Monte Carlo simulation, Phys. D: Appl. Phys. 41 (2008) 205307.